Surface reactivity and cation non-stoichiometry in $BaZr_{1-x}Y_xO_{3-\delta}$ (x=0-0.2) exposed to CO_2 at elevated temperature

Rokas Sažinas[a,b,c], Martin F. Sunding[d], Annett Thøgersen[d], Isao Sakaguchi[b], Truls Norby[e], Tor Grande[a], Jonathan M. Polfus[d*]

[a] Department of Materials Science and Engineering, NTNU Norwegian University of Science and Technology, NO-7491 Trondheim, Norway
[b] Research Center for Functional Materials, National Institute for Materials Science, 1-1 Namiki, Tsukuba 305-0044, Japan
[c] Department of Energy Conversion and Storage, Technical University of Denmark, DK-4000, Roskilde, Denmark
[d] SINTEF Industry, Sustainable Energy Technology, PO Box 124, Blindern, NO-0314 Oslo, Norway
[e] Department of Chemistry, University of Oslo, Centre for Materials Science and Nanotechnology (SMN), FERMiO, Gaustadalléen 21, NO-0349 Oslo, Norway

*Contact email: jonathan.polfus@sintef.no

Abstract

The reactivity of $BaZr_{1-x}Y_xO_{3-\delta}$ (x=0-0.2) ceramics under 1 atm CO_2 at 650 °C for up to 1000 h was investigated in order to elucidate possible degradation processes occurring when the material is applied as proton-conducting electrolyte in electrochemical devices. The annealed ceramics were characterized by a range of techniques (SEM, TEM, GIXRD, XPS and SIMS) with respect to changes in phase composition and microstructure. Formation of $BaCO_3$ was observed on the surfaces of the annealed samples and the amount increased with time and was higher for the Y-doped compositions. The subsurface regions were found to be deficient in Ba and, in the case of the Y-doped compositions, enriched in Y in two distinct chemical states as identified by XPS. First-principles calculations showed that these were Y residing on the Zr and Ba-site, respectively, and that local enrichment of Y both in bulk and on the surface attained a structure similar to Y_2O_3. Overall, it was substantiated that the reaction with CO_2 mainly proceeded according to a defect chemical reaction ~~involing~~ involving transfer of Y to the Ba-site and consumption of $BaZrO_3$ formula units. It was suggested that a similar degradation mechanism may occur in the case of $Ba(OH)_2$ formation under high steam pressure conditions.

1. Introduction

$A^{II}B^{IV}O_3$ perovskites have been widely studied as materials for solid state electrochemical devices.[1-3] Alkali earths such as strontium and barium on the A-site implies the possibility of reaction with CO_2 to form stable carbonates at low to intermediate temperatures in electrochemical systems for conversion of hydrocarbons[1, 3-10]. The CO_2-sensitivity of the

materials can originate from thermodynamic phase instability or surface reactivity, and minor compositional modifications can affect the chemical stability.[11] Consequently, traditional solid-state reaction synthesis can be insufficient to avoid compositional heterogeneities that exhibit poorer resistance to CO_2 [11] and powder processing can therefore also have a significant impact on stability as well as sinterability.[12, 13, 14]

The high proton conductivity of Y-doped $BaZrO_3$ (BZY) has made BZY the state-of-the-art solid state electrolyte in proton ceramic fuel cells (PCFCs)[3, 15] and electrochemical membrane reactors.[16, 17] BZY has a cubic crystal structure,[18] and BZY containing 10 mol% yttria (BZY10) has become one of the most studied compositions.[19] Ce-containing compositions, $BaZr_{1-x-y}Ce_xY_yO_3$ (BZCY), possess higher proton conductivity and improved sintering properties.[20] However, the chemical stability towards CO_2-, H_2O-, or H_2S-containing atmospheres is reduced with increasing Ce-content.[21]

The presence of carbonate can have significant effect on the transport properties of proton conductors,[22, 23] as well as on the catalytic activity in the presence of hydrocarbons.[9] Nevertheless, a recent study by Duan et al. showed excellent coking resistance and sulfur tolerance of $BaZrO_3$-based PCFCs.[24] Structural and chemical degradation has been reported even in yttria stabilized zirconia (YSZ) in carbon-rich fuel gases such as CH_4, CO or syngas, inducing coking/graphitization and (oxy)carbide formation[25-28] that led to irreversible changes in the transport properties.[27, 28] Thus, a thorough understanding of potential degradation processes at the surface of BZY materials is highly desirable, and could lead to valuable insights into the surface chemistry and structure of this important proton-conducting electrolyte.

While bulk BZY has been shown to be chemically stable in 1 atm CO_2 above about 600 °C in accordance with thermodynamic considerations,[29, 30] the surface of the material may still exhibit some reactivity. Computational studies have recently shown that CO_2 exhibits strong chemisorption on $BaZrO_3$ surfaces by formation of carbonate species and that a carbonate overlayer of $BaCO_3$ can be thermodynamically preferred even in 400 ppm CO_2 above 100 °C.[31] The reactivity between BZY and pure CO_2 has been demonstrated to result in formation of $BaCO_3$ and deterioration of the mechanical properties at 550-750 °C.[32] It was determined that the reaction with CO_2 resulted in Ba-deficiency in the exposed surface rather than formation of ZrO_2 crystallites,[32] and the reaction could thereby reasonably be described according to

$$Ba_{Ba}^{\times} + O_O^{\times} + CO_2(g) \rightarrow v_{Ba}'' + v_O^{\bullet\bullet} + BaCO_3(s) \qquad (1)$$

where v_{Ba}'' and $v_O^{\bullet\bullet}$ denote Ba- and O-vacancies, respectively, in Kröger-Vink notation.[33] Similar degradation has also been reported for Sr-based perovskites.[5, 34] Alternative reaction pathways can be hypothesized based on further consideration of the phase stability and cation defect chemistry of BZY. In this respect, the coexistence of a Y-rich composition has been reported within single grains of Ba-deficient BZY.[35-37] Han et al. showed by synchrotron X-ray diffraction that excess Y can occupy the A-site, i.e., $Y_{Ba}^{\bullet}$.[18] Another possible reaction mechanism between BZY and CO_2 towards $BaCO_3$ and Ba-deficient BZY can therefore be expressed by relocation of Y from the Zr to the Ba site and consumption of one $BaZrO_3$ formula unit according to

$$2Ba_{Ba}^{\times} + Y_{Zr}' + 2O_O^{\times} + v_O^{\bullet\bullet} + 2CO_2(g) \xrightarrow{-BaZrO_3} Y_{Ba}^{\bullet} + 2BaCO_3(s) \quad (2)$$

In this study, we present a thorough investigation of the reactivity of dense $BaZr_{1-x}Y_xO_{3-\delta}$ (x=0-0.2) ceramics with CO_2 as the gas relevant for anodic fuel conversion electrochemical devices. The BZY samples were exposed to 1 atm CO_2 at 650 °C for 10-1000 h, and the extent of $BaCO_3$ formation and changes in the BZY surface microstructure and chemical composition were investigated by several techniques. Reactions (1) and (2) both result in Ba-deficient BZ(Y) according to the change in A/B-site ratios, Ba/Zr and Ba/(Zr+Y), respectively. However, the reactions may be differentiated by presence of the $Y_{Ba}^{\bullet}$ species as well as the level of deterioration of the BZY grains due to the consumption of a $BaZrO_3$ formula unit in Reaction (2). Furthermore, density functional theory (DFT) calculations were performed to evaluate relevant point defect energetics and to compare the thermodynamic feasibility Reaction (1) and (2).

2. Experimental

2.1 Sample preparation

Dense $BaZr_{1-x}Y_xO_{3-\delta}$ (x=0-0.2) ceramics were prepared by the procedure described in two recent contributions.[32, 38] Powders made by spray pyrolysis (CerPoTech, Norway) were calcined at 950 °C for 12 h, ball milled and pressed into pellets by uniaxial pressing followed by cold isostatic pressing at 200 MPa. The pellets were sintered at 1600 °C for 10 h in a powder bed consisting of 90 wt% BZY and 10 wt% $BaCO_3$. The pellets were polished with SiC papers and diamond suspensions down to 1 µm in order to obtain surfaces with low roughness. The density of the materials was measured by the Archimedes method using isopropanol at room temperature. The polished disc samples were broken into several pieces and annealed under 1 atm of dry flowing CO_2 at 650 °C for total exposure times of 10, 20, 100 and 1000 h. The 10 and 20 h annealing experiments were performed in an alumina tube furnace, and the longer annealings of 100–1000 h were performed in a ProboStat measurement cell (NORECS, Norway) with a sample holder of alumina and platinum wires. The samples are identified by their yttrium content (BZ, BZY10 and BZY20 for 0, 10 and 20% Y doping, respectively) and their exposure time to CO_2 at 650 °C.

X-ray powder diffraction (XRD) of the calcined powders and sintered materials was performed using a Bruker D8 Advance DaVinci diffractometer using $CuK_{\alpha 1}$ radiation. Grazing incidence XRD (GIXRD) was performed using $CuK_{\alpha 1}$ and parallel beam optics on pristine samples and samples exposed to CO_2 to characterize the formation of $BaCO_3$ on the surface. Rietveld refinement of the XRD patterns for powders was carried out using the TOPAS V4.1 software using a cubic structure model ($Pm\bar{3}m$) for all the materials.

The microstructure of the materials was investigated with Hitachi S3400N and Hitachi FEG Zeiss Ultra scanning electron microscopes (SEM) on gold coated samples. The chemical composition of phases was investigated by energy dispersive spectroscopy (EDS) with Oxford Instruments AZtec Energy analysis software.

2.2 Transmission electron microscopy

Cross-sectional transmission electron microscopy (TEM) samples were made using a focused ion beam on a dual-beam JEOL SEM. TEM was carried out using a FEI Titan G2 60-300 operated at 300 kV with high brightness XFEG, probe corrector, Gatan imaging filter for electron energy loss spectroscopy (EELS) analysis and super-X EDS detector. EELS results were acquired with STEM spectral imaging, using dual EELS, acquiring both high loss and low loss, for energy referencing.

2.3 Secondary ion mass spectrometry

The distribution of the isotopes was measured by secondary ion mass spectrometry (SIMS) using a Cameca IMS 4f instrument. A primary ion beam of 10 keV Cs^+ was applied while qualitative optimization of sputtering and mass intensity was performed with a 12.5 keV O_2^+ ion beam. The primary ion current varied between 30-60 nA, and the secondary ion intensity ranged between 5-6 nA. Depending on the secondary ion intensities, an area with a diameter of ~30 μm in the center of a sputtered 100 × 100 μm^2 area was gated for signal detection and analysis in order to avoid negative interferences (edge and wall effects). An electron shower with acceleration of 4.5 kV for ~1.2 mA sample current was used to charge compensate the insulating samples. Dynamic transfer optics setting (DTOS) of 60% was used. The secondary molecular ion signals were measured as function of the cycles per second (cps) and sputter time.

2.4 X-ray photoelectron spectroscopy

X-ray photoelectron spectroscopy (XPS) was performed on both pristine and CO_2-exposed BZY10 samples using a Kratos Axis Ultra^{DLD} XPS system with an incident monochromated Al Kα X-ray beam. The working pressure in the XPS chamber at room temperature was below 5×10^{-9} mbar. High resolution scans were recorded for the Ba 3d and 4d, Zr 3d, Y 3d, O 1s and C 1s energy regions, with a step size of 0.1 eV. All of the obtained binding energies (BE) were calibrated based on the C 1s peak for aliphatic bonds from adventitious carbon, set to 284.8 eV BE. The resulting XPS data were analysed using the CasaXPS software. A Gaussian-Lorentzian line shape GL(30) was employed to fit the XPS peaks after background subtraction based on the Shirley algorithm. The peak separation and area ratio of the Y $3d_{5/2}$ and the Y $3d_{3/2}$ peaks were constrained to be 2.05 eV and 3:2, respectively.

3. Computational methods

Y-doped $BaZrO_3$ was modeled as a 3 × 3 × 3 supercell (135 atoms) containing 4 yttrium acceptors and 2 oxygen vacancies for charge neutrality, corresponding to a dopant concentration of approx. 15% (denoted BZY15). Interactions between Y'_{Zr} and $v_O^{\bullet\bullet}$ were thereby taken into account for a specific configuration of the highly doped material. The binding energies between isolated defects were calculated based on the single fully ionized defects in 4 × 4 × 4 supercells. The BZY15 cell was constructed with a pair of Y'_{Zr} on next neighbor sites and two Y'_{Zr} on second next neighbor sites. Based on the calculated association energy between isolated Y'_{Zr} and $v_O^{\bullet\bullet}$ of -0.29 eV, the two charge-compensating $v_O^{\bullet\bullet}$ were placed in the most stable neighboring sites to Y'_{Zr}. The same procedure was followed for

introducing additional barium Schottky defect pairs, or the introduction of two $Y_{Ba}^{\bullet}$ and removal of the least stable $v_O^{\bullet\bullet}$, according to Eq. 1 and 2, respectively. The tendency for the defects to segregate to the surface was investigated using 11-layer (0 0 1) BaO-terminated slabs with 3 × 3 expansion perpendicular to the surface. Defect segregation energies were calculated as the total energy difference between charge neutral cells with the defects residing in the bulk and surface regions, respectively. The entropies of the reactions in Eq. 1 and 2 were estimated from tabulated entropies of CO_2 and the defect-free solid phases.[39, 40]

The DFT calculations were performed with VASP[41] based on the projector-augmented wave (PAW) method[42] and the generalized gradient approximation (GGA) functional due to Perdew, Burke and Ernzerhof.[43] Geometric optimization of the Y-doped supercell was performed with a 500 eV plane-wave energy cut-off and the subsequent calculations of the Ba-deficient cells were performed with fixed lattice parameters to represent bulk continuation to the surface. A 2 × 2 × 2 Monkhorst-Pack scheme was used for k-point sampling of the supercells.[44] The ionic positions were relaxed until the residual forces were within 0.05 eV $Å^{-1}$, while the self-consistent electronic optimization was performed with an energy convergence criterion of 10^{-6} eV. Core level shifts for Y 3d in the different configurations and clusters were obtained according to the initial state approximation as implemented in VASP.

4. Results

4.1 Formation of $BaCO_3$

The extent of $BaCO_3$ formation on the surface of BZ and BZY samples after annealing in CO_2 at 650 °C for 10 to 1000 h was investigated by GIXRD and SEM. Figure 1a and 1b show the GIXRD patterns of the pristine and annealed specimens. For both compositions, reflections corresponding to $BaCO_3$ (Pmcn) appear after annealing, and the amount of $BaCO_3$ increases with annealing time. On the other hand, there is no clear evidence of formation of ZrO_2 other than possibly small amounts for the BZY10 sample after 1000 h. Based on the relative intensities of the main reflections, the formation of $BaCO_3$ was more prominent in the Y-doped composition. As shown in the insets, there is a continuous shift of the BZ and BZY Bragg reflections towards smaller lattice parameters with increasing annealing time and $BaCO_3$ formation. Figure 1c and 1d show the surface of BZY10 before and after exposure to CO_2 at 650 °C for 10 h. Crystals of $BaCO_3$ were formed on the surface by exposure to CO_2, resulting in a rough surface. The average size of the crystals was about 4 μm.

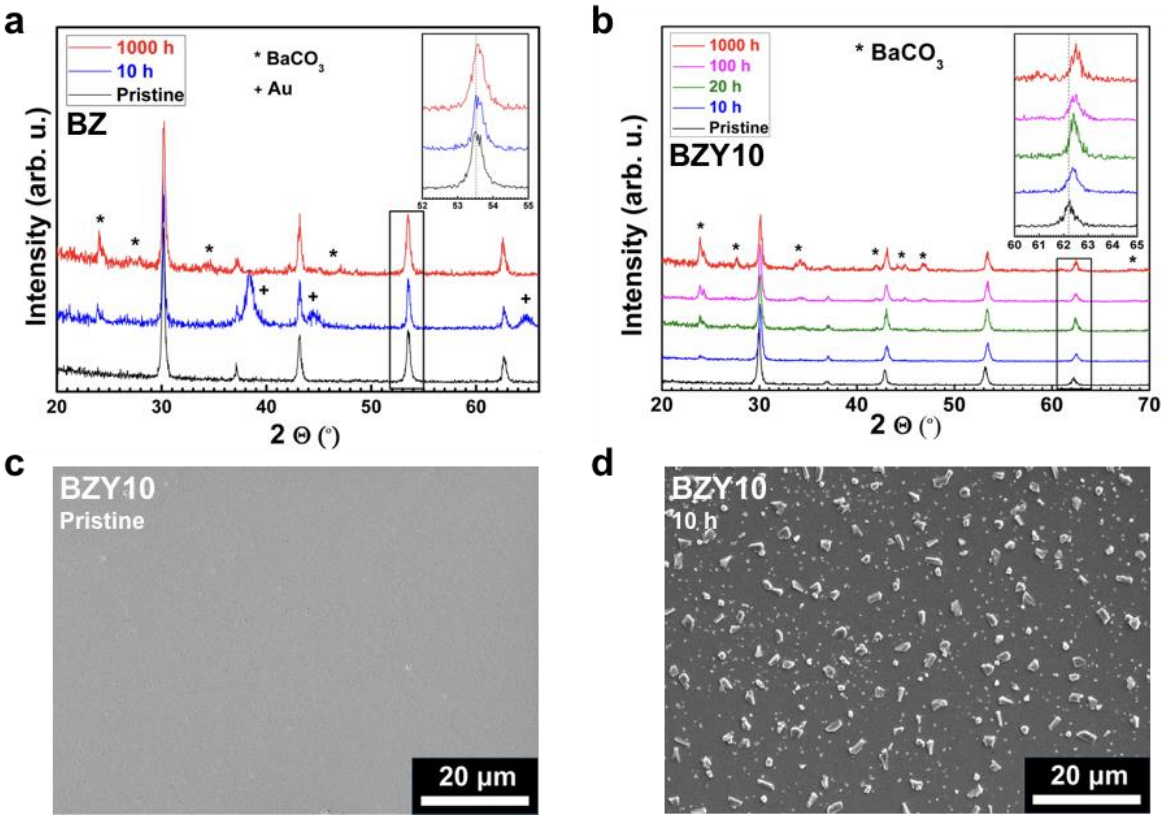

Figure 1: GIXRD patterns of BZ (a) and BZY10 (b) after CO_2 exposure at 650 °C for 10-1000 h, and SEM micrographs of the BZY10 surface before (c) and after exposure to CO_2 at 650 °C for 10 h (d).

4.2 Cation depth profiles

Figure 2a and b show cross-section EDS line scans of BZY10 as a function of depth from the surface for different annealing times normalized to the Zr-signal. The barium line scans show a clear deficiency towards the surface, which increases with increasing annealing time. The yttrium concentration profile in Figure 2b appears relatively constant throughout the analyzed region with no significant variations as a function of annealing time. The same result was observed when Y was normalized to the nominal B-site ratio, i.e., Y/(Zr+Y) ratio (not shown).

SIMS analyses were performed on the BZ and BZY samples annealed in CO_2 at 650 °C for 1000 h. The depth profiles of the elements normalized to Zr intensity are given in Figure 2c and d. According to these profiles, the BZ sample exhibits Ba-deficiency at the surface, while BZY10 and BZY20 seem to be quite stoichiometric. However, considering Y-segregation to the surface region shown in Figure 2b, the normalization to Zr does not reveal a consistent A/B-ratio due to the change in all of the elements from surface towards the bulk.

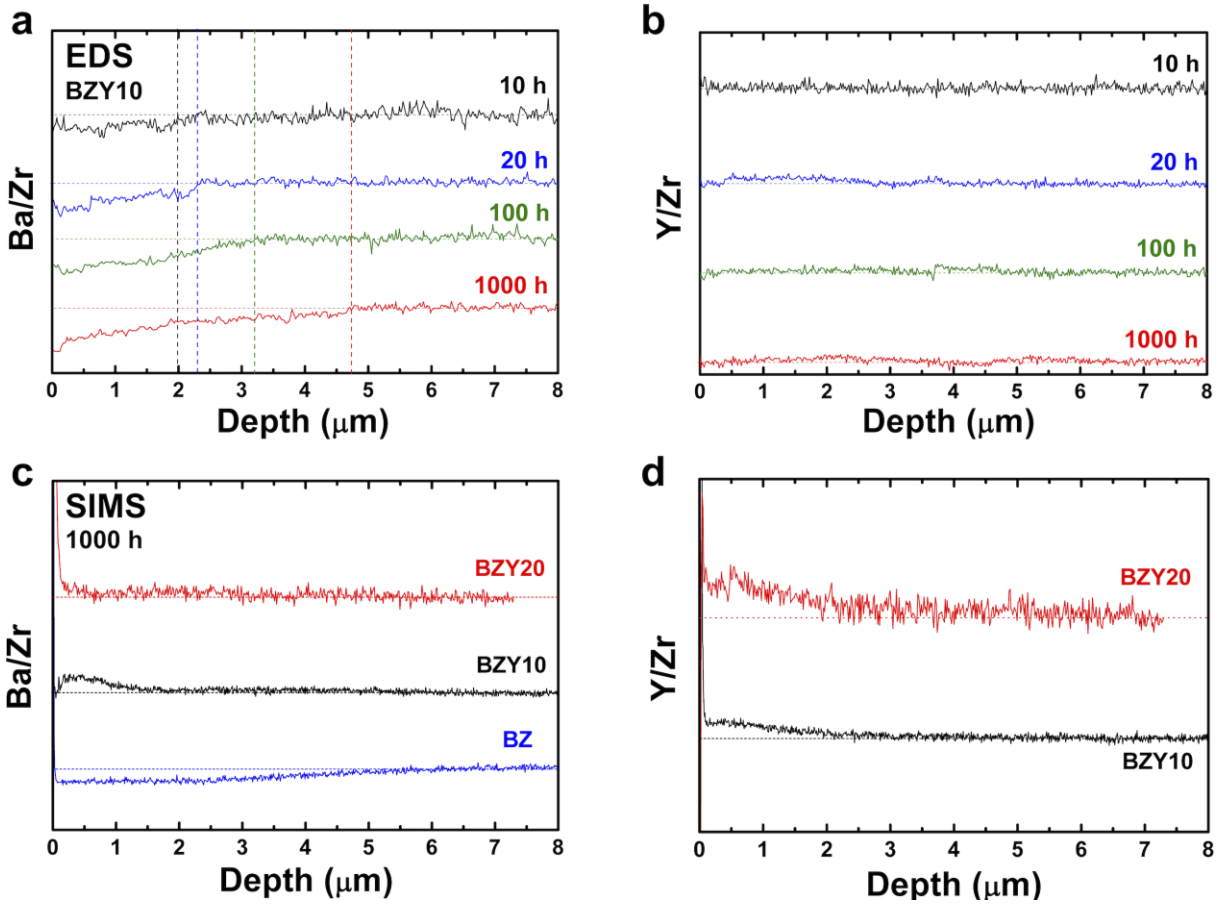

Figure 2: Cross-section EDS line scans of BZY10 as function of depth from the surface for different annealing times: A/B-site ratio (a), and Y/B-site ratio (b). The SIMS depth profiles of Ba (c) and Y (d) normalized to the Zr intensity in BZ, BZY10 and BZY20 annealed in CO_2 for 1000 h.

The carbon concentration profiles in BZY10 are shown in Figure 3. The amount and depth of carbon increase as a function of annealing time in CO_2. Due to the low atomic number, the carbon intensities were quite low compared to the intensities of Ba, Y and Zr.

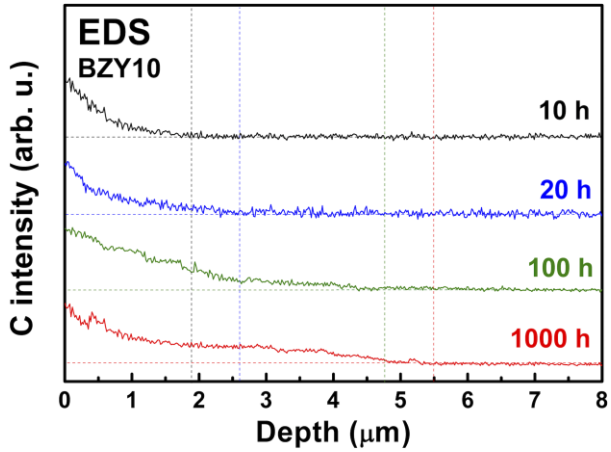

Figure 3: Concentration profile of C measured by EDS in BZY10.

4.3 TEM investigation of surface microstructure and phases

TEM was used to perform microstructure and phase characterization and in particular to investigate possible formation of secondary phases at the surface. Figure 4 shows a surface

cross-section TEM image of BZY10 annealed for 1000 h in CO_2 at 650 °C, and electron diffraction patterns from the surface region and 150 nm into the bulk. The grains corresponding to $BaCO_3$ are clearly visible on the surface. Other secondary phases like ZrO_2 or Y_2O_3 were not observed.

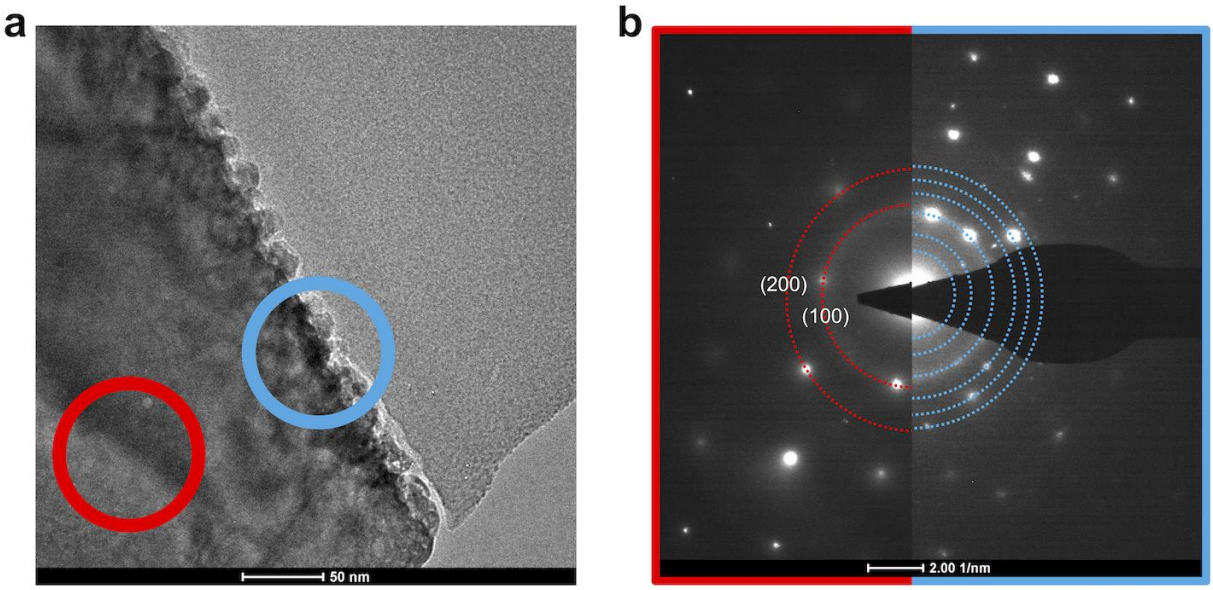

Figure 4: TEM cross-section image of the surface of the BZY10 (a) and diffraction patterns from surface and bulk (b).

The bulk (red) diffraction pattern shows the <100> zone axis of the BZY perovskite structure (Pm-3m) with a lattice parameter of 4.1 Å. The diffraction pattern from the surface (blue) shows the same crystal structure, albeit with a slightly increased lattice parameter of 4.4 Å, in addition to diffraction patterns from $BaCO_3$ and/or $Ba(OH)_2$. The increase in BZY lattice parameter might suggest a higher Y concentration in the top 150 nm. However, no difference in Y concentration was detected by EDS. One might speculate whether the apparent increase in C content towards the surface observed by EDS profiling may reflect interstitial carbon species and associated defects that expand the lattice. In this respect, DFT calculations have shown that carbon interstitials can be stabilized as carbonate species in either Ba- or Zr-vacancies in $BaZrO_3$.[22] While their equilibrium concentrations were determined to be negligible in acceptor doped material, the reaction may be facilitated by pre-existing cation vacancies as has been shown for dissolution of interstitial Ni into $BaZrO_3$ from NiO.[45]

In Figure 5a, a magnified high angled annular dark field (HAADF) STEM image shows that smaller pores of 5-20 nm were present inside the grains near the surface of BZY10 annealed for 1000 h in CO_2 at 650 °C. This is also shown in Figure 5b, in addition to structural dislocations. These nanoscopic voids exhibit high surface energies and cannot be expected to be stable after sintering of the material, and it is reasonable to assume that they may have been formed during the annealing in CO_2. This can point to Reaction (2), which involves consumption of $BaZrO_3$ formula units, rather than Reaction (1) which involves formation of Ba-deficient BZY. Additional HAADF images and electron energy loss spectroscopy (EELS) characterization is provided as Supplementary Information (SI).

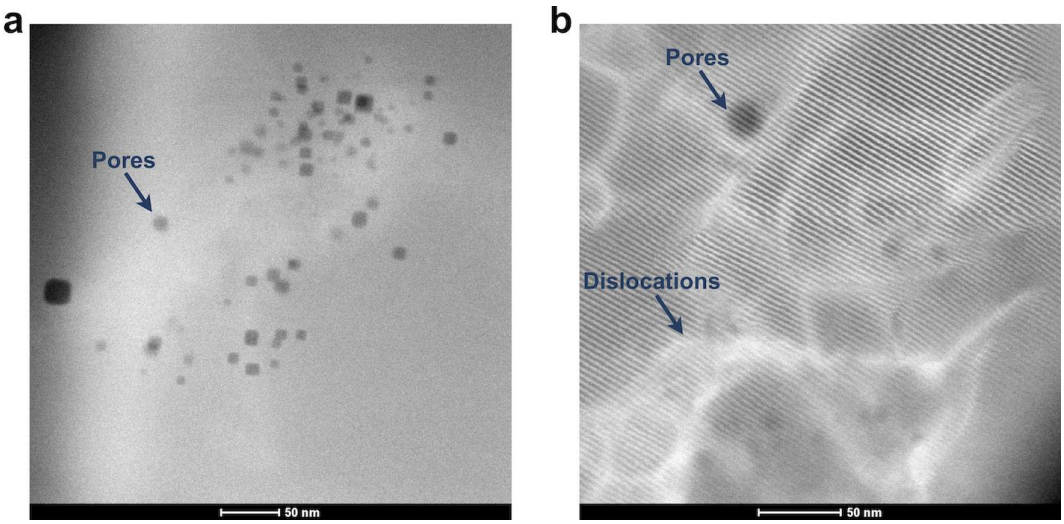

Figure 5: HAADF images of a) pores, and b) pores and dislocations in the material.

4.4 XPS and computational analyses of chemical states

XPS was performed to characterize changes in the chemical state of Y in the BZY samples after reaction with CO_2 to emulate possible formation of $Y_{Ba}^{\bullet}$ according to Reaction (2). The XPS spectra of Ba 4d and Y 3d are compared for BZY10 and BZY20 annealed in CO_2 for 100 h and 1000 h in Figure 6. The bulk spectra were taken from the annealed samples (1000 h) fractured under vacuum, and these may have been affected by long-range diffusion processes during the annealing although the main changes in stoichiometry were observed within 10 μm from the surface based on the EDS and SIMS profiles. The Ba 4d peak shows that at least two chemical states are present (Figure 6a). The lower binding energy (BE) peak can be related to BZY while the higher BE peak is typical for $BaCO_3$ and $Ba(OH)_2$. The intensity of the latter peak clearly increases with exposure time to CO_2, well in agreement with the $BaCO_3$ formation on the surface of BZY10 samples as detected by GIXRD and EELS (Figure S2). The Zr element is quite stable in CO_2 atmosphere, showing unchanged position of Zr 3d peaks with increasing exposure time (Figure S3). On the other hand, the Y 3d peak shows a complex structure that changes with increasing time of CO_2 exposure (Figure 6b,c). Two spin-orbit pairs describing at least two different chemical states were required for a satisfactory fitting of the Y 3d energy region. The spin-orbit pair at the highest BE exhibited a core level shift of about 2.5 eV relative to the pair at lowest BE for BZY10. In the case of BZY20, the core level shift was quite similar for the bulk, while it decreased to about 1.6 eV after exposure to CO_2 (Figure 6c). The peak intensities for the chemical state at lower BE decreased with CO_2 exposure time in favor of the chemical state at higher BE (particularly evident for BZY20).

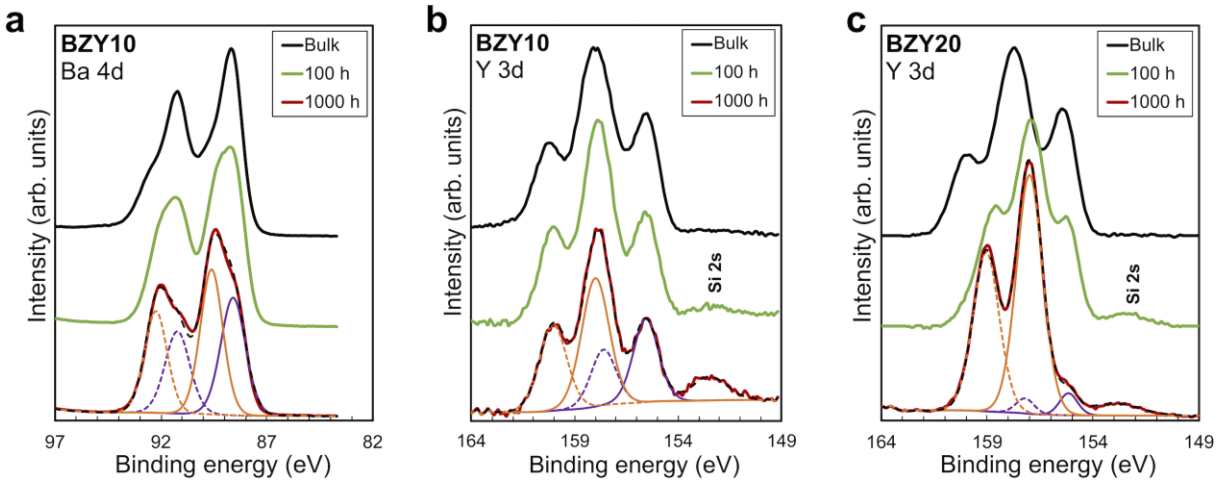

Figure 6: High resolution XPS (a) BZY10 Ba 4d, (b) BZY10 Y 3d and (c) BZY20 Y 3d spectra for the bulk (black), and the surface of the 100 h (green) and 1000 h (red) annealed samples.

The relative Y 3d core level shift of various Y defects and clusters was investigated computationally for comparison with results from XPS. Figure 7 shows several configurations of Y'_{Zr} (Figure 7b-d) and $Y^{\bullet}_{Ba}$ (Figure 7e-g) with the calculated Y 3d core level shifts (Δ) relative to the fully coordinated Y'_{Zr} octahedra. The Y 3d core level shift for Y'_{Zr} associated with a protonic defect, a nearest neighbor Y'_{Zr} and/or an oxygen vacancy was 0.18-0.88 eV to higher binding energy relative to the isolated Y'_{Zr}. In comparison, the core level shift for $Y^{\bullet}_{Ba}$ was more significant, 2.21-2.40 eV towards higher binding energy. Similar Y 3d core level shifts were obtained for Y'_{Zr} and $Y^{\bullet}_{Ba}$ defects and clusters on the (0 0 1) BaO-terminated surface, i.e., there was no significant difference between the core level shifts for bulk and surface.

Despite the rather large difference in size between Y and 12-coordinated Ba, $Y^{\bullet}_{Ba}$ attained a 6-coordinated configuration by relaxing towards the edge (Figure 7**Error! Reference source not found.**f) or face (Figure 7g) of the unit cell. The resulting Y-O bond lengths, 2.3-2.4 Å, were similar to those for the various configurations of Y'_{Zr}, 2.1-2.3 Å. Notably, the local structure surrounding $Y^{\bullet}_{Ba}$ resembled that of Y_2O_3 ($Ia\bar{3}$) comprising distorted YO_6 octahedra and three-coordinated oxide ions similar to Figure 7e-g. Overall, Y exhibited distinctly different 3d core level shifts when substituted on the Ba and Zr-site in $BaZrO_3$: 0-0.88 eV to higher binding energy for Y'_{Zr} and about 2.3 eV to higher binding energy for $Y^{\bullet}_{Ba}$. The difference in chemical shift of 1.4-2.3 eV between Y'_{Zr} and $Y^{\bullet}_{Ba}$ species corresponds well with the separation of about 1.6-2.5 eV observed by XPS. In the case of dehydrated material due to dry atmosphere, and a relatively low concentration of oxygen vacancies due to Reaction (2), the calculated shift would be closer to 2.4 eV (Figure 7a and e).

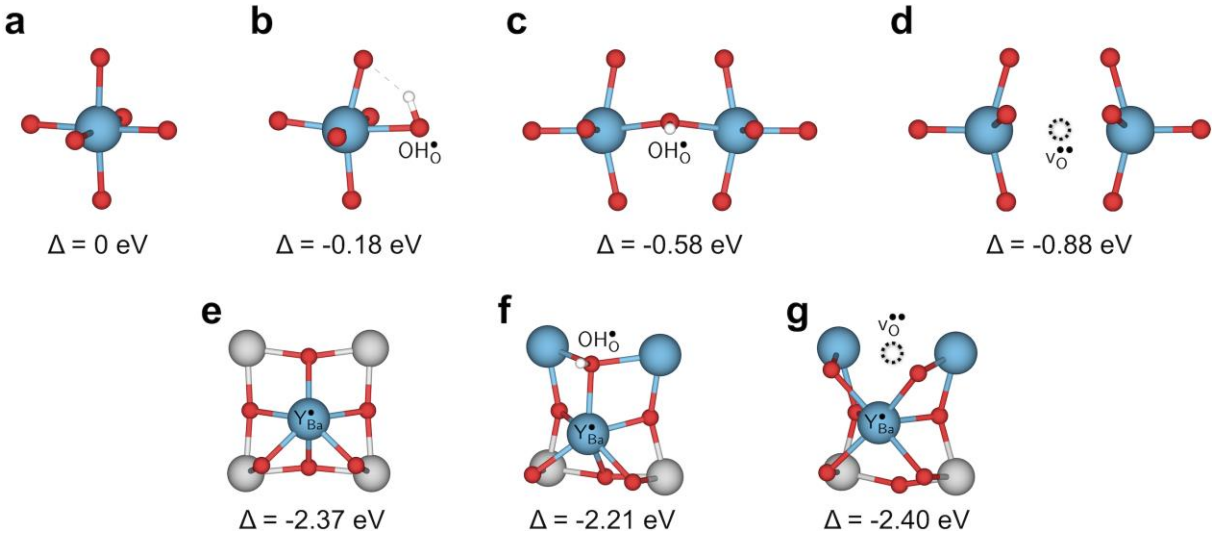

Figure 7: Local structural environment and Y 3d core level shift (Δ) for various configurations of Y'_{Zr} (a-d) and $Y^{\bullet}_{Ba}$ (e-g) from 3 × 3 × 3 supercells.

4.5 DFT calculations of reaction thermodynamics

DFT calculations were used to calculate and compare the enthalpy of Reactions (1) and (2), while the reaction entropies were estimated from the tabulated entropies of CO_2 and the solid phases. The relaxed structures of the computational cells with optimized configuration of additional defects are shown in **Error! Reference source not found.**Figure 8. The BZY15 reference cell, shown in Figure 8a, contains one oxygen vacancy in between two nearest-neighbor Y'_{Zr}, i.e., $(Y_{Zr} - v_O - Y_{Zr})^{\times}$, and one oxygen vacancy associated with a single Y'_{Zr}.

The cell in Figure 8b contains a Schottky pair where the most favored site for v''_{Ba} was adjacent to the $(Y_{Zr} - v_O - Y_{Zr})^{\times}$ complex, with the oxygen vacancies associated with the remaining fully coordinated Y'_{Zr}. The cell in Figure 8c contains two $Y^{\bullet}_{Ba}$, both of which were found to be most stable adjacent to $(Y_{Zr} - v_O - Y_{Zr})^{\times}$.

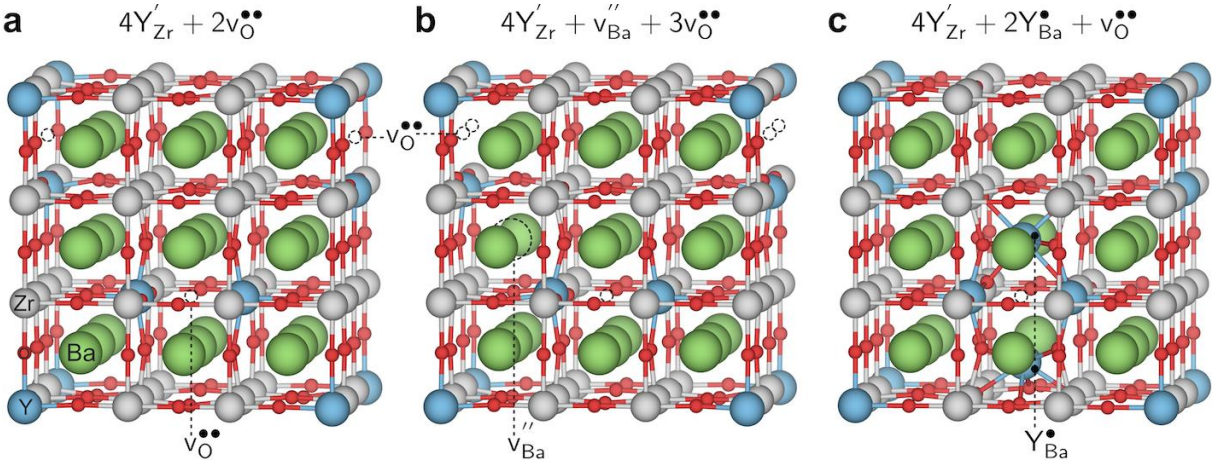

Figure 8: Relaxed structures of the initial defective cell containing 4 Y-acceptors and 2 oxygen vacancies (a), the Ba-deficient cell containing an additional barium Schottky pair (b), and the Y-rich cell containing 2 Y on Ba-site (c).

The total energy differences between the cells in Figure 8b and c with respect to the reference cell in Figure 8a were used to evaluate the enthalpies of Reaction (1) and (2). Table 1 shows the calculated Gibbs energies for the reactions at 650 °C based on cells containing different

amounts of defects as indicated by the degree of Ba-deficiency, *x*. While the obtained Gibbs energy of Reaction (1) was positive for all the considered cells and configurations, it was significantly lower and close to zero for Reaction (2). This indicates that Reaction (2) involving formation of $BaCO_3$ by accommodating Ba-deficiency and Y-enrichment in the bulk perovskite structure – and hence consumption of $BaZrO_3$ – can occur to a significant extent at 650 °C in 1 atm CO_2.

Table 1: Thermodynamic parameters for the Reactions (1) and (2) at 650 °C showing the defects formed and consumed in the reactions, and the extent of Ba-deficiency (*x*) in the defective cells. The reaction enthalpies were obtained from DFT and the reaction entropies were estimated from tabulated entropies of CO_2 and the solid phases.

Reaction	Defects	*x*	ΔH / eV	$T\Delta S$ / eV	ΔG / eV
1	$v''_{Ba} + v^{\bullet\bullet}_{O}$	0.040	0.29	-1.26	1.55
		0.070	0.40		1.66
		0.110	0.55		1.81
2	$2Y^{\bullet}_{Ba} - v^{\bullet\bullet}_{O}$	0.016	-1.89	-1.86	-0.03
		0.074	-1.92		-0.06

The tendency for yttrium to segregate to the surface was evaluated for BaO-terminated (0 0 1). The calculated segregation energy of $Y^{\bullet}_{Ba}$ was -0.33 eV, indicating a considerable stabilization of the defect at the surface, shown in Figure S4 (SI). The segregation energy for an additional Y'_{Zr} to the $Y^{\bullet}_{Ba}$ at the surface was -0.50 eV, resulting in an overall segregation energy of -0.82 eV for the associated defect pair from the bulk to the surface (see SI for additional details).

5. Discussion

Observations by several techniques (SEM, TEM, GIXRD) show that $BaCO_3$ crystallites form on the surfaces of BZ and BZY after annealing in 1 atm CO_2 at 650 °C. The amount of $BaCO_3$ increases with annealing time from 10 to 1000 h and it becomes larger for Y-doped compositions. The surface becomes Ba-deficient based on SIMS and SEM-EDS analysis for BZ and BZY, respectively. (It is difficult to assess Ba-stoichiometry in BZY by SIMS since there is no constant reference due to simultaneous changes in the Y and Zr contents). The Ba-deficiency reaches several micrometers into the material, and it is likely that Ba is transported along grain boundaries.[46] Moreover, the corresponding carbon profile from SEM-EDS indicates $BaCO_3$ formation along grain boundaries and/or dissolution of carbon species into the perovskite.

The BZY surfaces become enriched in Y as indicated by SIMS and XPS, and the Y-enrichment appears to extend several micrometers into the material, i.e., similar to the corresponding deficiency in Ba. XPS show two distinctly different chemical states of Y, which based on DFT calculations were identified as Y substituted on the A site, $Y^{\bullet}_{Ba}$, and B site, Y'_{Zr}, respectively. Furthermore, the DFT calculations indicate that these Y-species tend to cluster, both in the bulk and at the surface. The resulting local enrichment in Y becomes structurally similar to Y_2O_3 and may explain previous observations of Y-rich regions within

BZY grains.[35-37] The changes in stoichiometry near the surface is accompanied by a substantial increase in lattice parameter of the remaining perovskite, as observed by TEM.

All in all, formation of $BaCO_3$ on BZY in CO_2 atmosphere at 650 °C appears to mainly proceed according to Reaction (2), in which Y'_{Zr} ends up as a charge compensating donor, $Y^{\bullet}_{Ba}$, while a $BaZrO_3$ formula unit is consumed. The latter fits with the observation of small intragrain pores by TEM and the general absence of Y_2O_3 or ZrO_2 secondary phases. In comparison to BZ, where $BaCO_3$ formation is lower, the Y-dopant thereby provides an extra compositional degree of freedom that facilitates $BaCO_3$ formation according to Reaction (2).

Now, the question is to what extent the formation of $BaCO_3$ by Reaction (2) will proceed. Under the conditions used it is possible that it will proceed until complete decomposition to $BaCO_3$ and for instance Y-saturated ZrO_2, and Zr-saturated Y_2O_3 or other compounds for BZY with higher Y-dopant concentrations. This process will take thousands of h before completion, while larger BZY grains will probably retard the transport of Ba to the surface and hence also the decomposition and degradation. Another alternative is that it stops by equilibrium when a certain content of $Y^{\bullet}_{Ba}$ is reached. The observation that there is a certain Ba-deficiency and Y excess quite far into the material – instead of complete decomposition at the very surface – may support this alternative. These and other degradation paths could be studied by the reaction between for instance $BaCO_3$ and YSZ in 1 atm CO_2.

In any case, while we have shown that BZY suffers severe $BaCO_3$ formation in 1 atm CO_2 and probably degradation of its functional and thermomechanical properties, many applications of BZY electrolytes may not be significantly affected. Lower CO_2 partial pressures or impurity levels of CO_2 should mitigate the degradation processes in hydrogen fuel cells and steam electrolyzers. However, such devices operating at steam pressures within the stability regime of $Ba(OH)_2$ may exhibit similar degradation phenomena and mechanisms as we have observed here.[47]

A recent study on CO_2 and H_2O coadsorption has shown preferential adsorption of H_2O on BZY and indicated that the presence of H_2O prevents the formation of a carbonate overlayer on BZY surfaces.[48] For applications with high CO_2 partial pressures due reforming of hydrocarbons, the presence of steam may therefore limit the $BaCO_3$ formation and the associated degradation processes. Further degradation studies should take into account both CO_2 and H_2O. Temperatures lower than 650 °C are desirable for many applications of BZY, which worsens the thermodynamics of stability but slows down diffusion, so the effect of temperature may go both ways.

6. Conclusions

Over a time-scale of 1000 h, $BaZr_{1-x}Y_xO_{3-\delta}$ (x=0-0.2) ceramics exhibit severe degradation under 1 atm CO_2 at 650 °C due to formation of $BaCO_3$ on the surfaces and possibly along the grain boundaries, accompanied by Ba-deficiency in the subsurface regions. For the Y-doped compositions, the surface and subsurface become enriched in Y, which may be ascribed to a degradation reaction in which Y ends up on the Ba-site while $BaZrO_3$ formula units are consumed. Accordingly, the degradation proceeds faster with Y as an additional compositional degree of freedom and a more favourable degradation reaction. The local enrichment of Y both in the bulk and on the surface attains a structure similar to Y_2O_3. Electrochemical devices based on Y-doped $BaZrO_3$ electrolytes may be stable towards

$BaCO_3$ formation under lower CO_2 partial pressures and/or in the presence of H_2O, while further work is necessary to be conclusive.

7. Acknowledgements

Financial support from The Research Council of Norway under the program NANO2021 to the project “Functional oxides for clean energy technologies: fuel cells, gas separation membranes and electrolysers” (FOXCET, 228355) conducted by SINTEF, University of Oslo and The Norwegian University of Science and Technology (NTNU), is gratefully acknowledged in addition to FME NCCS (257579). Computational resources were provided by the Norwegian Metacenter for Computational Science (NOTUR) under the project nn9259k.

8. References

1. J. W. Phair, S. P. S. Badwal, "Materials for separation membranes in hydrogen and oxygen production and future power generation" *Sci.Tech. Adv. Mater.*, **7** (2006) 792-805.
2. D. A. Medvedev, J. G. Lyagaeva, E. V. Gorbova, A. K. Demin, P. Tsiakaras, "Advanced materials for SOFC application: Strategies for the development of highly conductive and stable solid oxide proton electrolytes" *Progr. in Mater. Sci.*, **75** (2016) 38-79.
3. N. Kochetova, I. Animitsa, D. Medvedev, A. Demin, P. Tsiakaras, "Recent activity in the development of proton-conducting oxides for high-temperature applications" *RSC Adv.*, **6** (2016) 73222-73268.
4. J. A. Kilner, M. Burriel, "Materials for Intermediate-Temperature Solid-Oxide Fuel Cells" *Ann. Rev. Materi. Res.*, **44** (2014) 365-393.
5. J. D. Baniecki, M. Ishii, K. Kurihara, K. Yamanaka, T. Yano, K. Shinozaki, T. Imada, K. Nozaki, N. Kin, "Photoemission and quantum chemical study of $SrTiO_3$(001)surfaces and their interaction with CO_2" *Phys. Rev. B*, **78** (2008).
6. J. LÜ, L. Wang, L. Fan, Y. Li, L. Dai, H. Guo, "Chemical stability of doped $BaCeO_3$-$BaZrO_3$ solid solutions in different atmospheres" *J. Rare Earths*, **26** (2008) 505-510.
7. X. Ma, J. Dai, H. Zhang, D. E. Reisner, "Protonic conductivity nanostructured ceramic film with improved resistance to carbon dioxide at elevated temperatures" *Surface and Coatings Technology*, **200** (2005) 1252-1258.
8. C. S. Tu, R. R. Chien, V. H. Schmidt, S. C. Lee, C. C. Huang, C. L. Tsai, "Thermal stability of $Ba(Zr_{0.8-x}Ce_xY_{0.2})O_{2.9}$ ceramics in carbon dioxide" *J. App. Phys.*, **105** (2009) 103504.
9. N. Zakowsky, S. Williamson, J. Irvine, "Elaboration of CO_2 tolerance limits of $BaCe_{0.9}Y_{0.1}O_{3-\delta}$ electrolytes for fuel cells and other applications" *Solid State Ionics*, **176** (2005) 3019-3026.
10. D. Medvedev, J. Lyagaeva, S. Plaksin, A. Demin, P. Tsiakaras, "Sulfur and carbon tolerance of $BaCeO_3$–$BaZrO_3$ proton-conducting materials" *J. Pow. Sour.*, **273** (2015) 716-723.
11. A. Brandão, J. F. Monteiro, A. V. Kovalevsky, D. P. Fagg, V. V. Kharton, J. R. Frade, "Guidelines for improving resistance to CO_2 of materials for solid state electrochemical systems" *Solid State Ionics*, **192** (2011) 16-20.
12. P. Duran, J. Tartaj, C. Moure, "Sintering behaviour and microstructural evolution of agglomerated spherical particles of high-purity barium titanate" *Ceram. Int.*, **29** (2003) 419-425.

13. B.-K. Yoon, E.-Y. Chin, S.-J. L. Kang, "Dedensification During Sintering of $BaTiO_3$ Caused by the Decomposition of Residual $BaCO_3$" *J. Am. Ceram. Soc.*, **91** (2008) 4121-4124.
14. I. Antunes, A. Brandão, F. M. Figueiredo, J. R. Frade, J. Gracio, D. P. Fagg, "Mechanosynthesis of nanopowders of the proton-conducting electrolyte material $Ba(Zr,Y)O_{3-\delta}$" *J. Solid State Chem.*, **182** (2009) 2149-2156.
15. K. D. Kreuer, "Proton-Conducting Oxides" *Ann. Rev. Mater. Res.*, **33** (2003) 333-359.
16. H. Malerød-Fjeld, D. Clark, I. Yuste-Tirados, R. Zanón, D. Catalán-Martinez, D. Beeaff, S. H. Morejudo, P. K. Vestre, T. Norby, R. Haugsrud, J. M. Serra, C. Kjølseth, "Thermo-electrochemical production of compressed hydrogen from methane with near-zero energy loss" *Nature Energy*, **2** (2017) 923-931.
17. S. H. Morejudo, R. Zanon, S. Escolastico, I. Yuste-Tirados, H. Malerod-Fjeld, P. K. Vestre, W. G. Coors, A. Martinez, T. Norby, J. M. Serra, C. Kjolseth, "Direct conversion of methane to aromatics in a catalytic co-ionic membrane reactor" *Science*, **353** (2016) 563-566.
18. D. Han, K. Kishida, K. Shinoda, H. Inui, T. Uda, "A comprehensive understanding of structure and site occupancy of Y in Y-doped $BaZrO_3$" *J. Mat. Chem. A*, **1** (2013) 3027.
19. M. A. Laguna-Bercero, "Recent advances in high temperature electrolysis using solid oxide fuel cells: A review" *J. Pow. Sour.*, **203** (2012) 4-16.
20. D. Medvedev, A. Murashkina, E. Pikalova, A. Demin, A. Podias, P. Tsiakaras, "$BaCeO_3$: Materials development, properties and application" *Prog. Mater. Sci.*, **60** (2014) 72-129.
21. J.-W. Jhuang, K.-R. Lee, J.-k. Chang, C.-T. Shen, Y.-H. Lee, S.-W. Lee, C.-J. Tseng, "Chemical stability and electrical and mechanical properties of $BaZr_xCe_{0.8-x}Y_{0.2}O_3$ with CeO_2 protection method" *Int. J. Hydrogen Energy*, **42** (2017) 22259-22265.
22. F. Trobec, V. Thangadurai, "Transformation of proton-conducting Perovskite-type into fluorite-type fast oxide ion electrolytes using a CO_2 capture technique and their electrical properties" *Inorg Chem*, **47** (2008) 8972-8984.
23. A. L. Cabrera, F. Vargas, R. A. Zarate, "Adsorption of carbon dioxide by barium titanate: Evidence of adsorption process mediated by a dipole-dipole interaction" *J. Phys. and Chem. of Solids*, **55** (1994) 1303-1307.
24. C. Duan, R. J. Kee, H. Zhu, C. Karakaya, Y. Chen, S. Ricote, A. Jarry, E. J. Crumlin, D. Hook, R. Braun, N. P. Sullivan, R. O'Hayre, "Highly durable, coking and sulfur tolerant, fuel-flexible protonic ceramic fuel cells" *Nature*, **557** (2018) 217-222.
25. M. Kogler, E. M. Kock, T. Bielz, K. Pfaller, B. Klotzer, D. Schmidmair, L. Perfler, S. Penner, "Hydrogen Surface Reactions and Adsorption Studied on Y_2O_3, YSZ, and ZrO_2" *J. Phys. Chem. C Nanomater. Interfaces*, **118** (2014) 8435-8444.
26. E. M. Kock, M. Kogler, T. Bielz, B. Klotzer, S. Penner, "In Situ FT-IR Spectroscopic Study of CO_2 and CO Adsorption on Y_2O_3, ZrO_2, and Yttria-Stabilized ZrO_2" *J. Phys. Chem. C Nanomater. Interfaces*, **117** (2013) 17666-17673.
27. E. M. Kock, M. Kogler, T. Gotsch, B. Klotzer, S. Penner, "Structural and chemical degradation mechanisms of pure YSZ and its components ZrO_2 and Y_2O_3 in carbon-rich fuel gases" *Phys. Chem. Chem. Phys.*, **18** (2016) 14333-14349.
28. M. Kogler, E.-M. Köck, B. Klötzer, L. Perfler, S. Penner, "Surface Reactivity of YSZ, Y_2O_3, and ZrO_2 toward CO, CO_2, and CH_4: A Comparative Discussion" *J. Phys. Chem. C*, **120** (2016) 3882-3898.
29. K. H. Ryu, S. M. Haile, "Chemical stability and proton conductivity of doped $BaCeO_3$–$BaZrO_3$ solid solutions" *Solid State Ionics*, **125** (1999) 355-367.
30. E. Fabbri, A. D'Epifanio, E. Di Bartolomeo, S. Licoccia, E. Traversa, "Tailoring the chemical stability of $Ba(Ce_{0.8-x}Zr_x)Y_{0.2}O_{3-\delta}$ protonic conductors for Intermediate Temperature Solid Oxide Fuel Cells (IT-SOFCs)" *Solid State Ionics*, **179** (2008) 558-564.

31. J. M. Polfus, B. Yildiz, H. L. Tuller, R. Bredesen, "Adsorption of CO_2 and Facile Carbonate Formation on $BaZrO_3$ Surfaces" *J. Phys. Chem. C*, **122** (2018) 307-314.
32. R. Sažinas, C. Bernuy-López, M. A. Einarsrud, T. Grande, "Effect of CO_2 Exposure on the Chemical Stability and Mechanical Properties of $BaZrO_3$-Ceramics" *J. Am. Ceram. Soc.*, **99** (2016) 3685-3695.
33. F. A. Kröger, H. J. Vink, "Relations between the Concentrations of Imperfections in Crystalline Solids" *Solid State Phys.*, **3** (1956) 307-435.
34. I. Kaus, K. Wiik, B. Krogh, M. Dahle, K. H. Hofstad, S. Aasland, "Stability of $SrFeO_3$-Based Materials in H_2O/CO_2-Containing Atmospheres at High Temperatures and Pressures" *J. Am. Ceram.Soc.*, **90** (2007) 2226-2230.
35. Y. Yamazaki, R. Hernandez-Sanchez, S. M. Haile, "Cation non-stoichiometry in yttrium-doped barium zirconate: phase behavior, microstructure, and proton conductivity" *J. Mater. Chem.*, **20** (2010) 8158.
36. A. K. Azad, C. Savaniu, S. Tao, S. Duval, P. Holtappels, R. M. Ibberson, J. T. S. Irvine, "Structural origins of the differing grain conductivity values in $BaZr_{0.9}Y_{0.1}O_{2.95}$ and indication of novel approach to counter defect association" *J. Mater. Chem.*, **18** (2008) 3414.
37. F. Giannici, M. Shirpour, A. Longo, A. Martorana, R. Merkle, J. Maier, "Long-Range and Short-Range Structure of Proton-Conducting Y: $BaZrO_3$" *Chem. Mater.*, **23** (2011) 2994-3002.
38. R. Sažinas, M. A. Einarsrud, T. Grande, "Toughening of Y-doped $BaZrO_3$ proton conducting electrolytes by hydration" *J. Mater. Chem. A*, **5** (2017) 5846-5857.
39. M. Chase, "NIST-JANAF Thermochemical Tables, 4th Edition" *J. Phys. Chem. Ref. Data. Monograph*, (1998) 1952.
40. K. Kurosaki, R. J. M. Konings, F. Wastin, S. Yamanaka, "The low-temperature heat capacity and entropy of $SrZrO_3$ and $BaZrO_3$" *J. All. Comp.*, **424** (2006) 1-3.
41. G. Kresse, D. Joubert, "From ultrasoft pseudopotentials to the projector augmented-wave method" *Phys. Rev. B*, **59** (1999) 1758-1775.
42. P. E. Blöchl, "Projector augmented-wave method" *Phys. Rev. B*, **50** (1994) 17953-17979.
43. J. P. Perdew, K. Burke, M. Ernzerhof, "Generalized Gradient Approximation Made Simple" *Phys. Rev. B*, **77** (1996) 3865-3868.
44. H. J. Monkhorst, J. D. Pack, "Special points for Brillouin-zone integrations" *Phys. Rev. B*, **13** (1976) 5188-5192.
45. J. M. Polfus, M.-L. Fontaine, A. Thøgersen, M. Riktor, T. Norby, R. Bredesen, "Solubility of transition metal interstitials in proton conducting $BaZrO_3$ and similar perovskite oxides" *J. Mater. Chem. A*, **4** (2016) 8105-8112.
46. R. Sažinas, I. Sakaguchi, I. Hasle, J. M. Polfus, R. Haugsrud, M. A. Einarsrud, T. Grande, "Tracer diffusion of ^{96}Zr and ^{134}Ba in polycrystalline $BaZrO_3$" *Phys. Chem. Chem. Phys.*, **19** (2017) 21878-21886.
47. A. Slodczyk, M. D. Sharp, S. Upasen, P. Colomban, J. A. Kilner, "Combined bulk and surface analysis of the $BaCe_{0.5}Zr_{0.3}Y_{0.16}Zn_{0.04}O_{3-\delta}$ (BCZYZ) ceramic proton-conducting electrolyte" *Solid State Ionics*, **262** (2014) 870-874.
48. J. M. Polfus, J. Yang, B. Yildiz, "Interplay between H_2O and CO_2 coadsorption and space-charge on Y-doped $BaZrO_3$ surfaces" *J. Mater. Chem. A*, **6** (2018) 24823-24830.

Supplementary Information

Surface reactivity and cation non-stoichiometry in $BaZr_{1-x}Y_xO_{3-\delta}$ (x=0-0.2) exposed to CO_2 at elevated temperature

Rokas Sažinas[a,b,c], Martin F. Sunding[d], Annett Thøgersen[d], Isao Sakaguchi[b], Truls Norby[e], Tor Grande[a], Jonathan M. Polfus[d*]

[a] Department of Materials Science and Engineering, NTNU Norwegian University of Science and Technology, NO-7491 Trondheim, Norway
[b] Research Center for Functional Materials, National Institute for Materials Science, 1-1 Namiki, Tsukuba 305-0044, Japan
[c] Department of Energy Conversion and Storage, Technical University of Denmark, DK-4000, Roskilde, Denmark
[d] SINTEF Industry, Sustainable Energy Technology, PO Box 124, Blindern, NO-0314 Oslo, Norway
[e] Department of Chemistry, University of Oslo, Centre for Materials Science and Nanotechnology (SMN), FERMiO, Gaustadalléen 21, NO-0349 Oslo, Norway

*Contact email: jonathan.polfus@sintef.no

Figure S1 shows HAADF STEM images of the surface of BZY10 after 1000 h of exposure. The images show a rough surface, with crystalline particles of 10-15 nm in diameter. However, energy dispersive X-ray spectroscopy shows no variations in chemical composition between the particles and the bulk, in this area.

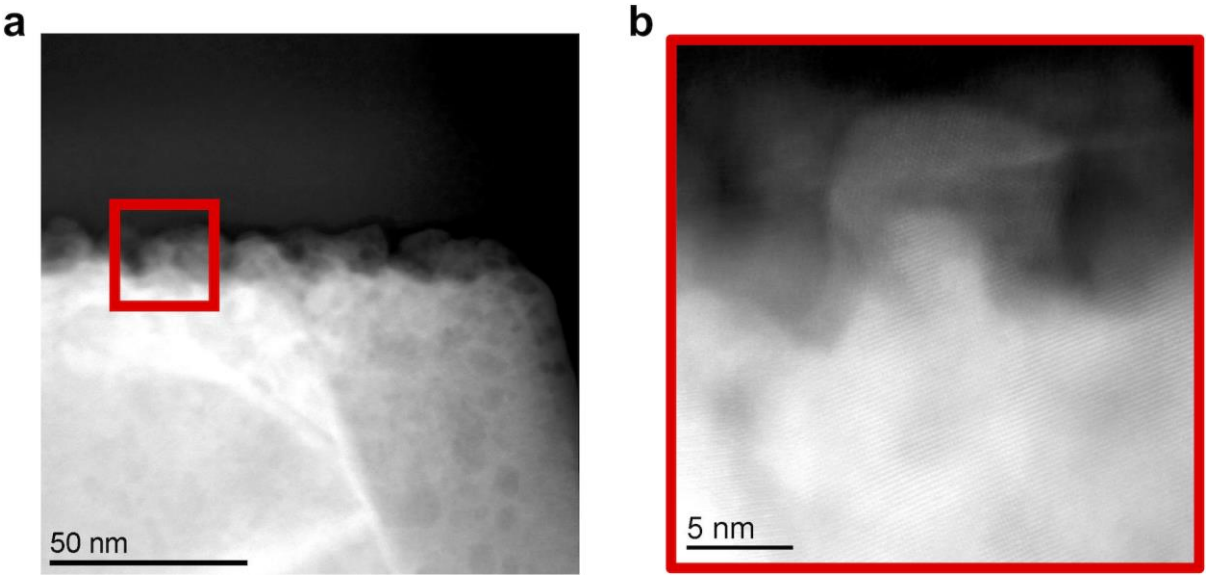

Figure S1: HAADF images of the particles on the surface of the film.

The chemical shift in the Ba peak within 300 nm of the surface was measured using electron energy loss spectroscopy (EELS). The results for Ba-M4,5 (3d) are shown in Figure S2 with the corresponding HAADF STEM image. The top 150 nm at the surface of the BZY sample

shows a 1.5 eV shift of the Ba-$M_{4,5}$ peak shift to a higher energy loss. This shift indicates a change in oxidation state and chemical structure.

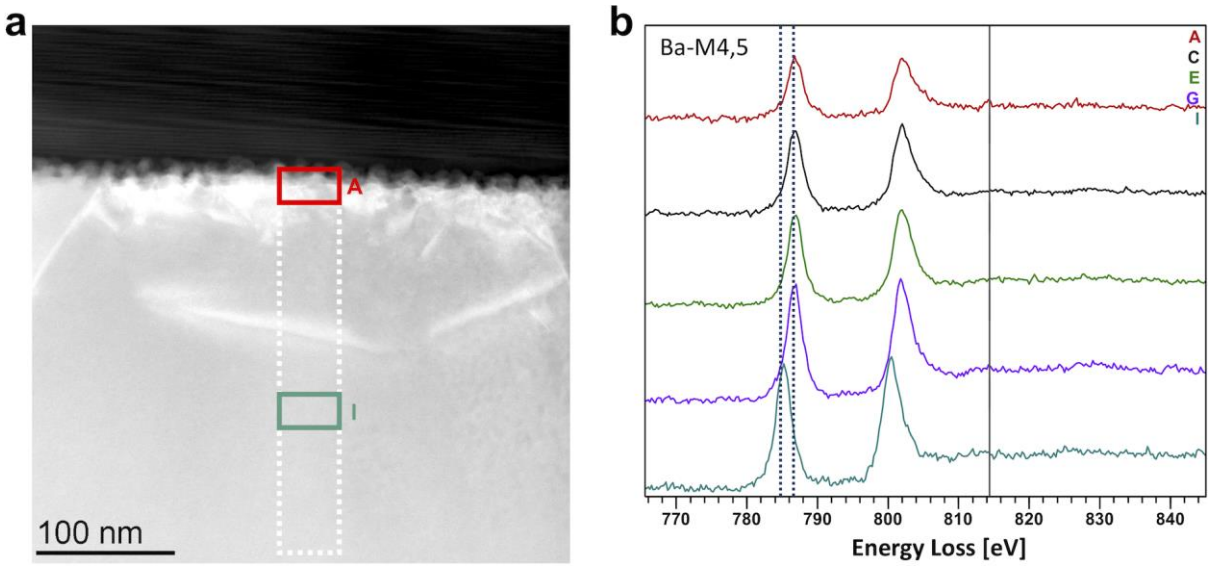

Figure S2: HAADF image of the surface of the films (a) and the corresponding EELS spectra (b).

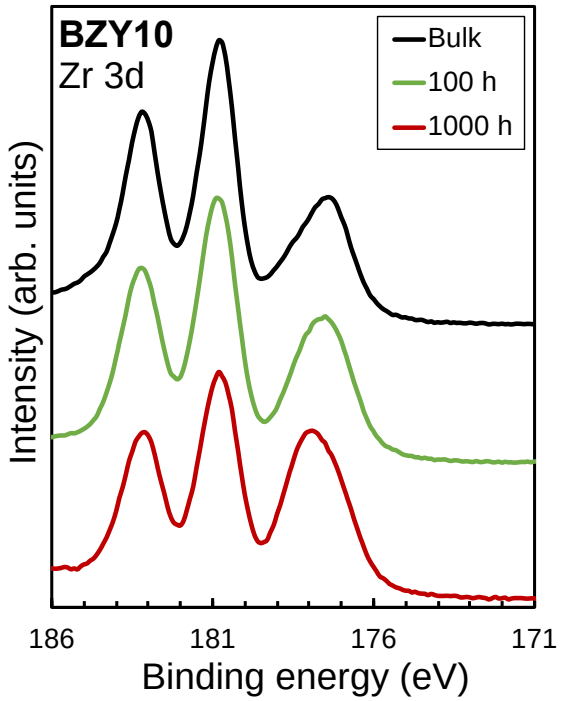

Figure S3: High resolution XPS Zr 3d spectra for the bulk (black), and the surface of the 100 h (green) and 1000 h (red) annealed BZY10 samples.

Surface segregation energies for defects were calculated as the total energy difference between charge neutral cells with the defects residing in the bulk and surface regions, respectively. Figure S4a shows the relaxed structure of $Y_{Ba}^{\bullet}$ on the BaO-terminated (0 0 1) surface, which exhibited a segregation energy for -0.33 eV. The segregation energy for an additional Y_{Zr}' to the $Y_{Ba}^{\bullet}$ at the surface was -0.50 eV, resulting in an overall segregation energy of -0.82 eV for the associated defect pair from the bulk to the surface. The overall segregation energy for a cluster of $Y_{Ba}^{\bullet} + Y_{Zr}' + v_O^{\bullet\bullet}$ was calculcated to -0.64 eV (**Error!**

Reference source not found.S4b). In this case, the cluster was most stable with $v_O^{\bullet\bullet}$ close to surface $Y_{Ba}^{\bullet}$ rather than as a $(Y_{Zr} - v_O - Y_{Zr})^{\times}$ cluster as was found for the bulk.

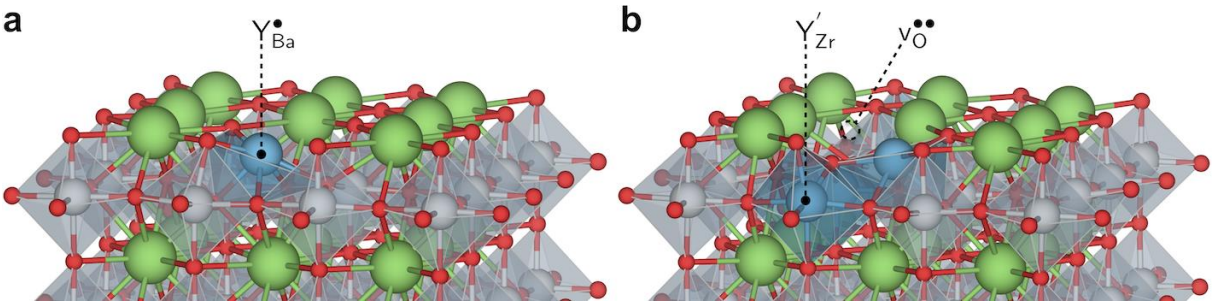

Figure S4: BaO-terminated (0 0 1) surface with segregated $Y_{Ba}^{\bullet}$ (a) and a cluster of two Y'_{Zr}, one $Y_{Ba}^{\bullet}$ and one $v_O^{\bullet\bullet}$.